Check for updates

Received: 14 February 2021 | Accepted: 30 March 2021

DOI: 10.1111/jace.17839

Journal of the American Ceramic Society

ORIGINAL ARTICLE

A low-permittivity microwave dielectric ceramic $BaZnP_2O_7$ and its performance modification

Xiaoqing Chen[1] | Hao Li[1] | Pengcheng Zhang[1] | Houlin Hu[1] | Gongtian Chen[2] | Gaosheng Li[1]

[1]College of Electrical and Information Engineering, Hunan University, Changsha, China

[2]College of Materials Science and Engineering, Hunan University, Changsha, China

Correspondence
Hao Li, College of Electrical and Information Engineering, Hunan University, Changsha, China.
Email: hli@hnu.edu.cn

Abstract

Complex pyrophosphates compounds have attracted much attention as promising candidates for substrate applications. In the work, a low-permittivity $BaZnP_2O_7$ ceramic was synthesized through solid-state reaction. The pure phase $BaZnP_2O_7$ was crystallized in the triclinic P−1 space group. Excellent microwave dielectric properties of the $BaZnP_2O_7$ ceramic with $\varepsilon_r = 8.23$, $Qf = 56170$ GHz, and $\tau_f = -28.7$ ppm/°C were obtained at 870°C for 4 h. The substitution of Mg^{2+} for Zn^{2+} was found to have positive effects on grain morphology and dielectric properties. Optimized performance of $\varepsilon_r = 8.21$, $Qf = 84760$ GHz, and $\tau_f = -21.9$ ppm/°C was yielded at 900°C for the $BaZn_{0.98}Mg_{0.02}P_2O_7$ ceramic. Intrinsic dielectric properties of $BaZn_{1-x}Mg_xP_2O_7$ ceramics were studied via Clausius–Mossotti equation and complex chemical bond theory.

KEYWORDS

$BaZnP_2O_7$, low-permittivity, microwave dielectric properties

1 | INTRODUCTION

The past few decades have witnessed an ever-growing scholarly interest in microwave dielectric ceramics with the rapid development of telecommunication.[1-4] Recently, there is a strong ongoing search for dielectric ceramics with a dielectric constant (ε_r) less than 15, a low dielectric loss (tan δ = 1/Q), and a near-zero temperature coefficient (τ_f) to meet the demands for microwave substrate applications.[5,6] Although traditional inorganic substrates such as Al_2O_3 possess excellent dielectric properties, the exploration for novel materials with superior dielectric properties and sintering behaviors continues today.

Pyrophosphates belong to typical low-permittivity compounds, in which $M_2P_2O_7$ possesses two kinds of structure according to the ionic radius of M that is a divalent cation.[7] The structure is recognized as thortveitite-type if the M ionic radius is less than 0.97 Å (M = Mn, Mg, Zn), while the structure converts to dichromate-type if the M ionic radius is larger than 0.97 Å (M = Ca, Sr, Ba). The dependence of dielectric properties on the phase composition of $M_2P_2O_7$ (M = Ca, Sr, Ba, Mn, Mg, Zn) was investigated by Bian et al.[8] and dielectric properties were ε_r = 6.1~8.4, Qf = 12300~53500 GHz, and τ_f = −23~−746 ppm/°C. Sutapun et al.[9] studied the substitution effect of Zn^{2+} at the Mn site of $Mn_2P_2O_7$, and found that the dopants of $Zn_2P_2O_7$ were diffused completely into the $Mn_2P_2O_7$ structure, forming solid solutions.

In recent years, many compounds with the general formula of $M2M1P_2O_7$ have been reported with excellent microwave dielectric properties and low sintering temperatures. Complex pyrophosphates compounds $M2M1P_2O_7$ (M2 = Ca, Sr; M1 = Zn, Cu) were investigated as low temperature co-fired ceramic (LTCC) materials due to their intrinsic low sintering temperatures.[10] In the past, the work of $BaZnP_2O_7$ was mainly focused on the luminescence properties.[11,12] In 2016, Xie et al.[13] prepared $BaZnP_2O_7$ ceramics through solid-state reaction and reported its dielectric properties: ε_r = 8.4, Qf = 27925 GHz, and τ_f = −56.7 ppm/°C. However, there are

 © 2021 The American Ceramic Society

no reports on the performance modification for $BaZnP_2O_7$ ceramics to date. Considering the little difference of ionic radius and electronegativity between Zn^{2+} (0.68 Å, S = 1.65) and Mg^{2+} (0.66 Å, S = 1.31), we decided to substitute Mg^{2+} for Zn^{2+} in $BaZnP_2O_7$ ceramics. In the work, we systematically investigated the phase composition, grain morphology, and microwave dielectric properties of $BaZnP_2O_7$ ceramics, and then discussed the influence of Mg^{2+} substitution for Zn^{2+} on the dielectric properties.

2 | EXPERIMENTAL

$BaZn_{1-x}Mg_xP_2O_7$ (x = 0, 0.01, 0.02, 0.04, 0.06) ceramics were fabricated via solid-state synthesis, adopting reagent-grade $BaCO_3$ (99.8%), ZnO (≥99.0%), $Mg(OH)_2{\bullet}4MgCO_3{\bullet}5H_2O$ (≥99.0%), and $NH_4H_2PO_4$ (≥99.0%). The powders were mixed by stoichiometry and then ground with ethyl alcohol and zirconia balls for 9 h. The powders, ethanol, and balls were milled at a mass ratio of 1:2:10. In the work, we adopted two kinds of zirconia balls (big balls with 6 mm in diameter and small ones with 3 mm in diameter) at a mass ratio of 1:1. After calcination at 800°C for 4 h, re-milled and then dried powders added with PVA (5 wt%) were pressed into a cylinder with a diameter of 12 mm and a height of 6 mm (pressure: 15 MPa). Eventually, samples were sintered at 830-930°C for 4 h.

X-ray powder diffraction (XRD, X'Pert Pro MPD) was performed to determine the phase composition of samples with Cu Kα radiation in the range of 10° <2θ < 120°, with a step size of 0.013°. The grain morphology characteristics were observed employing scanning electron microscopy (SEM, FEI Inspect F). A transmission electron microscope (TEM, FEI Tecnai G2 F20) was measured to obtain selected area electron diffraction (SAED) and high-resolution transmission electron microscopy (HRTEM). In order to identify the valence states of ions, the X-ray photoelectron spectroscopy (XPS, Thermo Scientific K-Alpha) was employed with monochromated Al Kα radiation. Hakki–Coleman method was adopted to test ε_r and Qf at about 12 GHz with a network analyzer (HP83752A). Additionally, τ_f was determined by

$$\tau_f = \frac{f_{85} - f_{25}}{f_{25}(85 - 25)} \times 10^6 (\text{ppm}/^\circ C) \quad (1)$$

where f_{25} and f_{85} were resonant frequencies tested at 25°C and 85°C, respectively.

3 | RESULTS AND DISCUSSION

$BaZnP_2O_7$ ceramics were characterized by XRD (Figure 1A), showing that the phase $BaZnP_2O_7$ was the only crystalline phase. In the range of 830°C to 890°C, diffraction peaks of samples were well matched with the standard pattern of $BaZnP_2O_7$ (JCPDS#77-0659), which crystallized in the triclinic structure with space group P−1. To clarify the crystal structure, powder diffraction data were refined using GSAS software based on the Rietveld method. The quality of refined patterns was assessed by profile factors (R_p), weighted profile factors (R_{wp}), and goodness of fit values (χ^2), as shown in Table 1. Figure 1B displays the refined pattern of the $BaZnP_2O_7$ ceramic, using the sample sintered at 850°C as an instance.

$BaZnP_2O_7$ possessed a special three-dimensional structure, as shown in Figure 2. The double-tetrahedral P_2O_7 served

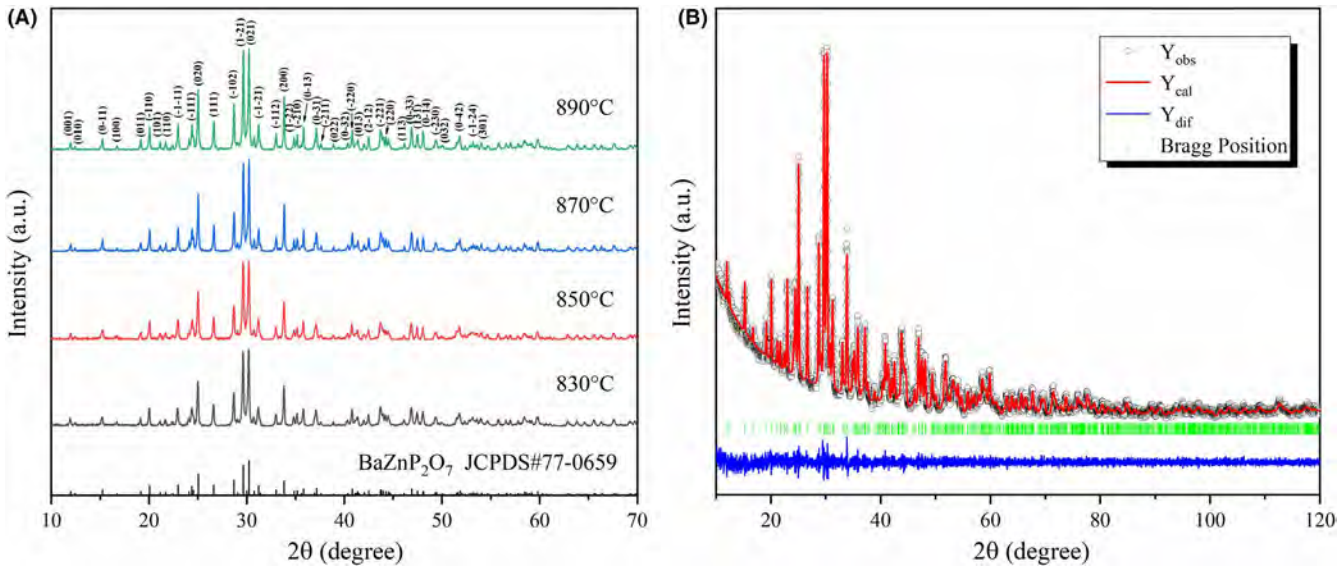

FIGURE 1 (A) The XRD patterns of $BaZnP_2O_7$ ceramics sintered at 830-890°C; (B) The refined pattern of the $BaZnP_2O_7$ ceramic sintered at 850°C

TABLE 1 Structural parameters and reliability factors of $BaZnP_2O_7$ ceramics

ST (°C)	830	850	870	890
a (Å)	5.3118(1)	5.3123(2)	5.3131(1)	5.3166(1)
b (Å)	7.3080(2)	7.3066(3)	7.3087(2)	7.3118(2)
c (Å)	7.5737(2)	7.5732(3)	7.5739(2)	7.5788(2)
α (°)	102.720(2)	102.722(3)	102.716(2)	102.721(2)
β (°)	92.125(2)	92.129(3)	92.123(2)	92.123(2)
γ (°)	94.066(3)	94.059(3)	94.080(2)	94.077(2)
V_{cell} (Å^3)	285.64(2)	285.59(3)	285.74(2)	286.24(2)
R_p (%)	4.48	4.38	4.59	4.55
R_{wp} (%)	5.84	5.69	6.01	5.93
χ^2	1.389	1.341	1.485	1.496

Abbreviation: ST: sintering temperature

FIGURE 2 The crystal structure of $BaZnP_2O_7$

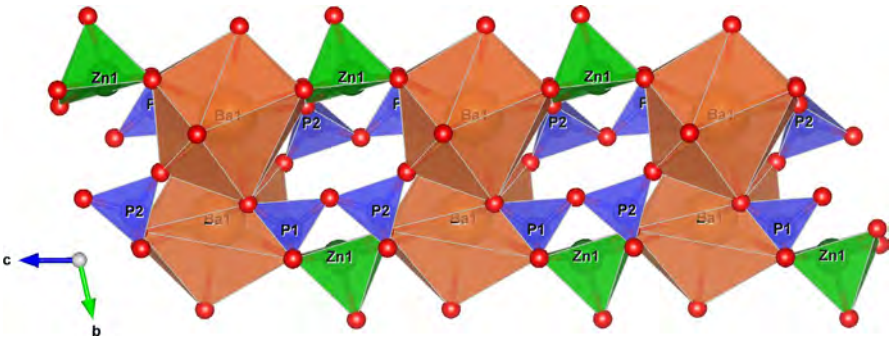

FIGURE 3 (A) The HRTEM image and (B) corresponding SAED pattern of the $BaZnP_2O_7$ ceramic sintered at 870°C along [010] zone axis

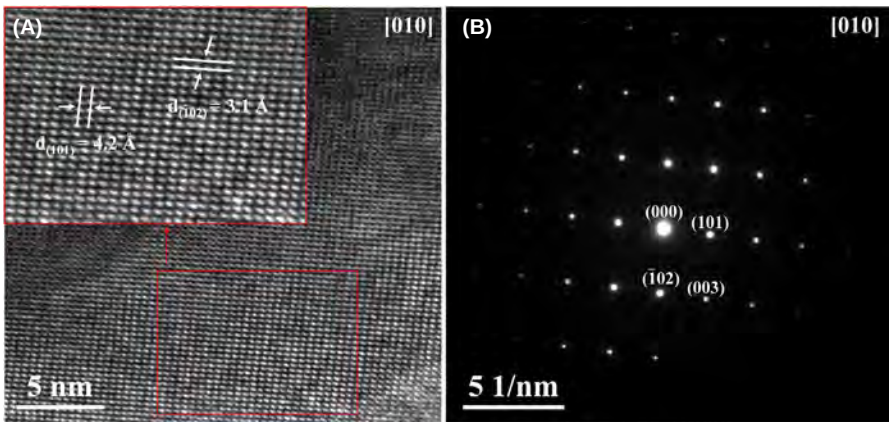

as a bridge among BaO_9 polyhedrons. Ba and Zn atoms were separately coordinated with nine and five O atoms, forming BaO_9 and ZnO_5 polyhedrons. P atoms showed two different crystallographic sites, that is, P1 and P2. P atoms were tetrahedrally coordinated with oxygen, forming almost regular PO_4 tetrahedrons with P-O bond lengths in the range of 1.492-1.607 Å. $P1O_4$ and $P2O_4$ tetrahedrons constituted a double-tetrahedral P_2O_7 via the corner-sharing O atom. We employed TEM analysis to further determine the structure of $BaZnP_2O_7$ ceramics. Figure 3 shows an HRTEM view and SAED pattern of the $BaZnP_2O_7$ ceramic sintered at 870°C, which were recorded along [010] zone axis. The HRTEM image showed the interplanar spacings of 4.2 and 3.1 Å, which matched well with the (101) and $(\bar{1}02)$ lattice planes of triclinic structure. The SAED pattern and HRTEM image were the supplements to XRD analysis, which confirmed that $BaZnP_2O_7$ belonged to the triclinic P−1 space group.

The chemical state of $BaZnP_2O_7$ ceramics was identified by XPS analysis. Figure 4A shows the existence of Ba 3d, Zn 2p, Zn LMM, P 2p, O 1s, and C 1s. The XPS peaks were calibrated with reference to C 1s peak of contamination carbon at 284.8 eV. The Ba 3d spectrum exhibited greatly separated spin-orbit $3d_{5/2}$ and $3d_{3/2}$ components (Δ = 15.3 eV) at 779.9 and 795.2 eV, which was indexed to Ba^{2+}.[14] Since the difference of Zn 2p peak positions between Zn^0 and Zn^{2+} was very small,[15,16] it was difficult to

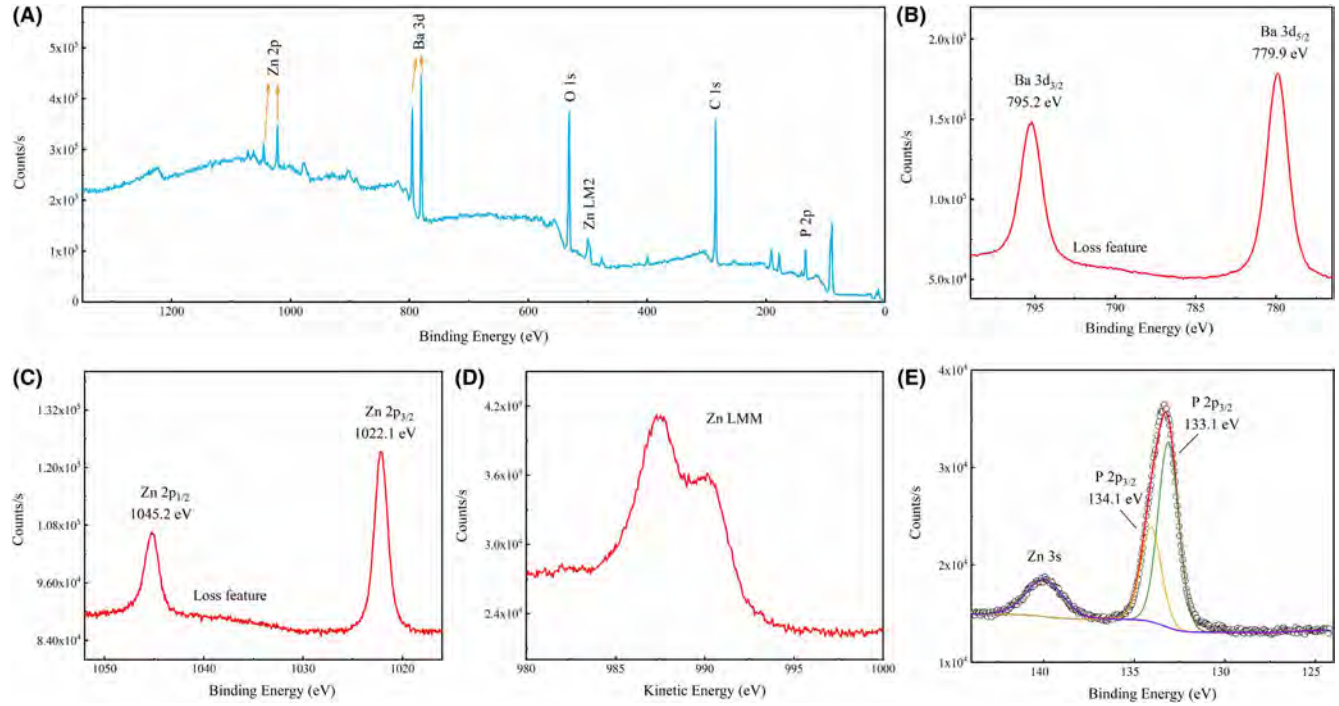

FIGURE 4 XPS spectra of the $BaZnP_2O_7$ ceramic sintered at 870°C with (A) the survey spectrum and high-resolution spectra of (B) Ba 3d, (C) Zn 2p, (D) Zn LMM, and (E) P 2p

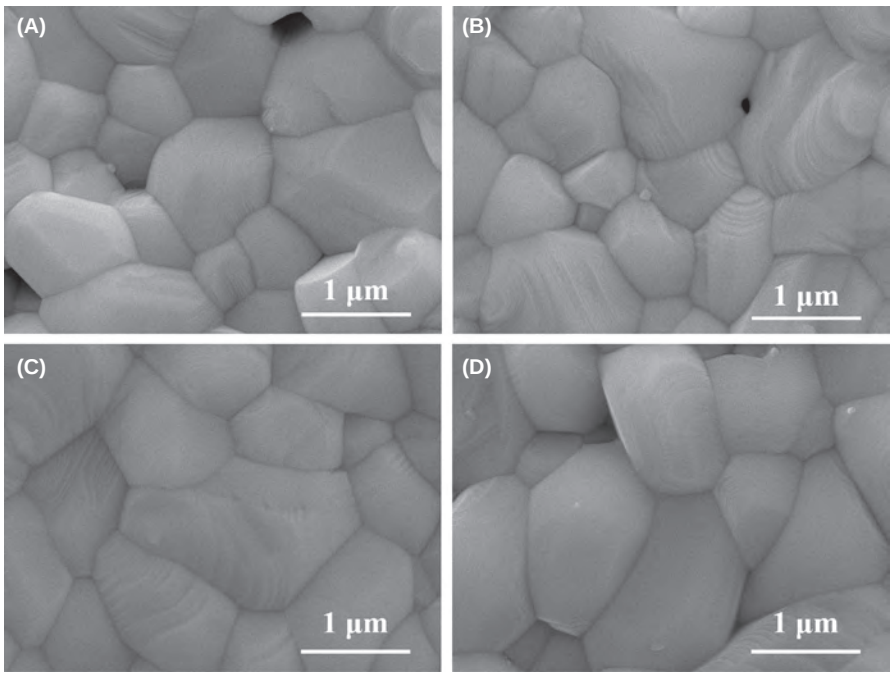

FIGURE 5 The SEM micrographs of $BaZnP_2O_7$ ceramics sintered at different temperatures for 4 h: (A) 830°C, (B) 850°C, (C) 870°C, and (D) 890°C

differentiate chemical states only with Zn 2p peaks (Figure 4C). Therefore, the Zn LMM Auger spectrum (Figure 4D) was also collected. The chemical state of Zn was assigned to Zn^{2+} due to the bigger chemical shifts of Zn^{2+} observed for Zn LMM compared to Zn^0. The P 2p spectrum had closely spaced spin-orbit components ($\Delta = 1.0$ eV), which was assigned to P^{5+}. Since zinc was present in the sample, it was reasonable to observe Zn 3 s peak at 140.0 eV.[17] The above analysis verified that the oxidation states of Ba, Zn, and P were +2, +2, and +5.

Figure 5 shows the surface SEM micrographs of $BaZnP_2O_7$ ceramics sintered at 830-890°C. With a rise in the sintering temperature, grains gradually grew and pores disappeared. The average grain size of $BaZnP_2O_7$ ceramics sintered at 830°C, 850°C, 870°C, and 890°C was 0.99 μm, 1.05 μm, 1.10 μm, and 1.11 μm, respectively. A dense and

homogeneous morphology with well-packed grains is observed in Figure 5C, corresponding to a low dielectric loss of the sample sintered at 870°C. With a further increase in the sintering temperature, the movement rate of grain boundary was faster than the diffusion rate of pores, which aroused a phenomenon that a few pores were trapped in ceramics at 890°C.

Figure 6A exhibits the change in relative density ($\rho_{relative}$) of $BaZnP_2O_7$ ceramics. Increasing sintering temperatures brought about an increase of $\rho_{relative}$, which reached a maximum value of 96.57% at 870°C. A slight decrease of $\rho_{relative}$ was observed with the further increase in the sintering temperature, which was in agreement with the microstructural observation. The change in ε_r was similar to that in $\rho_{relative}$, which indicated that porosity played a significant part in affecting the dielectric constant. The influence of pores on ε_r was described by spherical pore models as follows [18]:

$$\varepsilon_r = \varepsilon_{rc}\left(1 - \frac{3P\left(\varepsilon_{rc} - 1\right)}{2\varepsilon_{rc} + 1}\right) \quad (2)$$

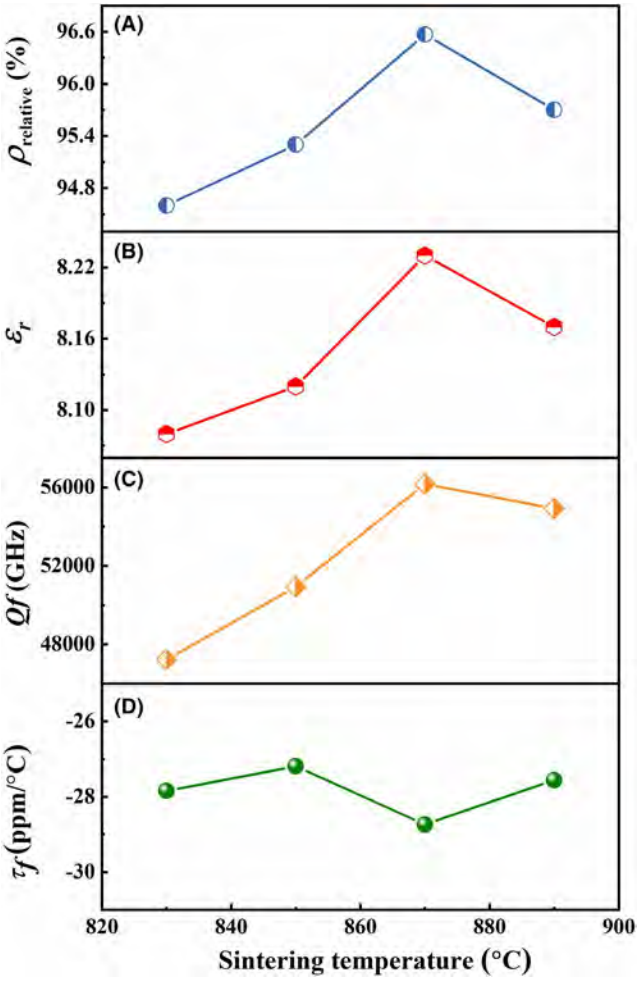

FIGURE 6 The changes in (A) $\rho_{relative}$, (B) ε_r, (C) *Qf*, and (D) τ_f of $BaZnP_2O_7$ ceramics

where ε_{rc} and P are porosity corrected ε_r and fractional porosity, respectively. Pores existed as a constituent ($\varepsilon_r \approx 1$), leading to the decrease in the permittivity of ceramics. Therefore, the highest ε_r of 8.23 was obtained for the sample sintered at 870°C due to the highest densification. Kucheiko et al.[19] reported that the *Qf* value was related to the average grain size. Pores and grain boundaries decreased with the increase in the average grain size, leading to the reduction in defects and the enhancement in *Qf* value. However, abnormal grain growth due to the over-high sintering temperature certainly deteriorated *Qf* value. Generally speaking, *Qf* value is affected by densification, average grain size, and anharmonic vibration.[20] As shown in Figure 6, the influence of densification was nonnegligible. As shown in Figure 6D, the τ_f of $BaZnP_2O_7$ samples sintered at 830-890°C fluctuated around −28 ppm/℃, showing a weak dependence on the sintering temperature. The phenomenon is common in other microwave dielectric ceramics, such as $NaCa_4V_5O_{17}$,[6] Li_2AGeO_4 (A = Zn, Mg),[21] and $AgCa_2B_2V_3O_{12}$ (B = Mg, Zn).[22]

The XRD patterns of $BaZn_{1-x}Mg_xP_2O_7$ (x = 0, 0.01, 0.02, 0.04, 0.06) samples sintered at optimum sintering temperatures are shown in Figure 7. In the range of $0.01 \leq x \leq 0.06$, the structure was indexed as triclinic (JCPDS#77-0659) with P−1 space group, suggesting that single-phase solid solutions were formed for all the samples. Figure 8 exhibits SEM micrographs of $BaZn_{1-x}Mg_xP_2O_7$ (x = 0.01, 0.02, 0.04, 0.06) ceramics, in which the compound surfaces were greatly dense. Homogeneous microstructures with few pores were observed for all the samples.

For pure-phase samples with high relative densities (>96%), the impact of extrinsic factors can be ignored. Therefore, the influence of dielectric polarizability on ε_r was discussed via Clausius–Mossotti equation.[23]

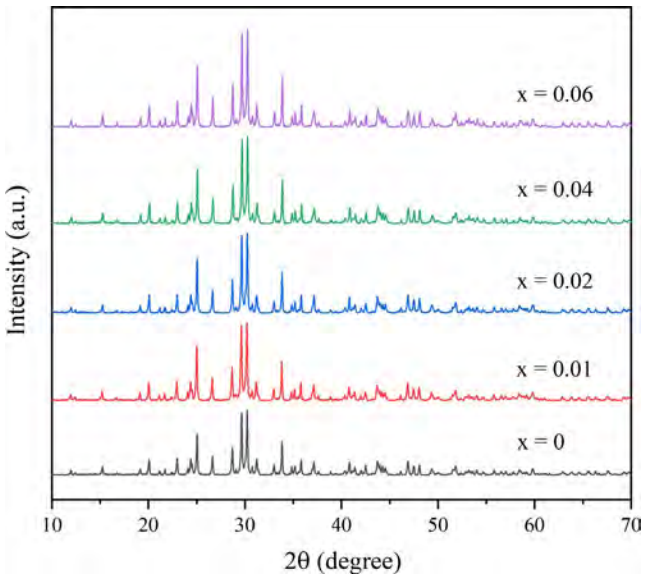

FIGURE 7 The XRD patterns of $BaZn_{1-x}Mg_xP_2O_7$ (x = 0, 0.01, 0.02, 0.04, 0.06) ceramics sintered at optimum temperatures

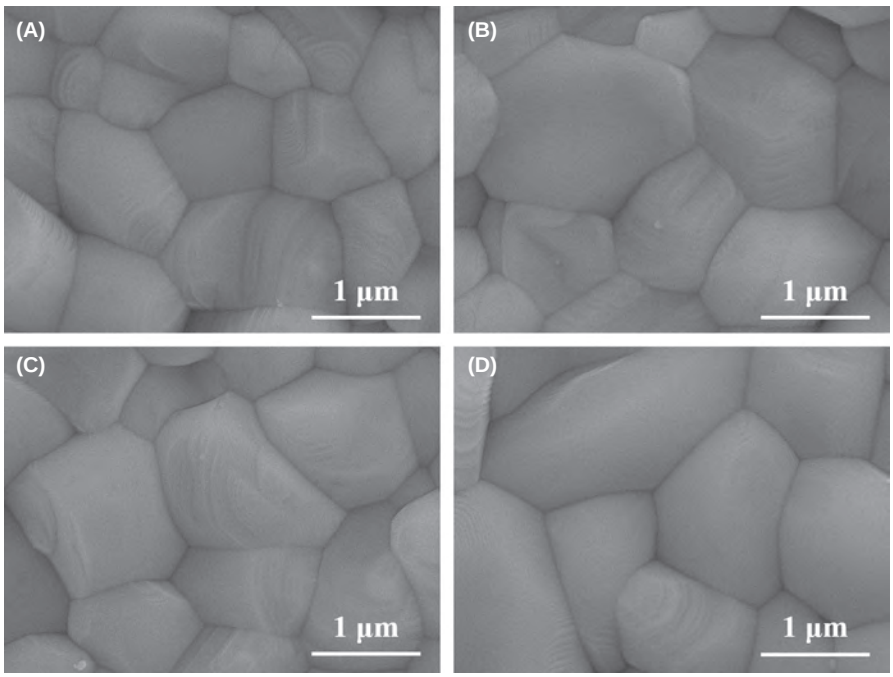

FIGURE 8 The SEM micrographs of $BaZn_{1-x}Mg_xP_2O_7$ ceramics sintered at optimum temperatures: (A) x = 0.01, (B) x = 0.02, (C) x = 0.04, and (D) x = 0.06

TABLE 2 Comparisons between α_{theo} and α_{obs} of $BaZn_{1-x}Mg_xP_2O_7$ ceramics

		Observed				
Compounds	α_{theo}	ε_r	V_{cell}	Z	α_{obs}	**Δ(%)**
$BaZnP_2O_7$	24.9500	8.23	286.129	2	24.1383	3.36
$BaZn_{0.99}Mg_{0.01}P_2O_7$	24.9428	8.22	285.745	2	24.0961	3.51
$BaZn_{0.98}Mg_{0.02}P_2O_7$	24.9356	8.21	285.624	2	24.0761	3.57
$BaZn_{0.96}Mg_{0.04}P_2O_7$	24.9212	8.19	284.637	2	23.9733	3.95
$BaZn_{0.94}Mg_{0.06}P_2O_7$	24.9068	8.15	284.518	2	23.9239	4.11

$$\alpha_{obs} = \frac{3V_m(\varepsilon_r - 1)}{4\pi(\varepsilon_r + 2)} \quad (3)$$

where ε_r and V_m are measured permittivity and molar volume (V_{cell}/Z). On the basis of additive rule,[24] the theoretical dielectric polarizability (α_{theo}) of $BaZn_{1-x}Mg_xP_2O_7$ samples obeys:

$$\alpha_{theo} = \alpha(Ba^{2+}) + (1-x)\alpha(Zn^{2+}) + x\alpha(Mg^{2+}) + 2\alpha(P^{5+}) + 7\alpha(O^{2-}) \quad (4)$$

where $\alpha(Ba^{2+})$ = 6.4 Å^3, $\alpha(Zn^{2+})$ = 2.04 Å^3, $\alpha(Mg^{2+})$ = 1.32 Å^3, $\alpha(P^{5+})$ = 1.22 Å^3, and $\alpha(O^{2-})$ = 2.01 Å^3, respectively.[23] Furthermore, the deviation (Δ) between α_{theo} and α_{obs} of $BaZn_{1-x}Mg_xP_2O_7$ was defined as follows:

$$\Delta = \left| \frac{\alpha_{theo} - \alpha_{obs}}{\alpha_{obs}} \times 100\% \right| \quad (5)$$

As shown in Table 2, the change in α_{theo} was consistent with that in α_{obs}, which suggested that the decline in ε_r was attributed to the lower ionic polarizability of Mg^{2+}, in comparison with Zn^{2+}. Furthermore, the calculated deviations (Δ) were so small (Table 2) that results were reliable.

The intrinsic dielectric properties of $BaZn_{1-x}Mg_xP_2O_7$ ceramics were investigated by the complex chemical bond theory. For a particular crystal structure, the unique bond lengths and bond angles lead to a variety of chemical and physical properties. After the classification of the A-O chemical bond (A = Ba, Zn, and P), $BaZnP_2O_7$ was decomposed into the following bond formula [25]:

$BaZnP_2O_7 = Ba_{1/18}O1(1)_{1/6} + Ba_{1/18}O1(2)_{1/6} + Ba_{1/9}O2(1)_{1/4} + Ba_{1/9}O2(2)_{1/4} + Ba_{1/9}O3_{1/4} + Ba_{1/9}O5(1)_{1/4} + Ba_{1/9}O5(2)_{1/4} + Ba_{1/9}O5(3)_{1/4} + Ba_{1/9}O6_{1/3} + Ba_{1/18}O7(1)_{1/4} + Ba_{1/18}O7(2)_{1/4} + Zn_{1/5}O1_{1/3} + Zn_{1/5}O2_{1/4} + Zn_{1/5}O3(1)_{1/4} + Zn_{1/5}O3(2)_{1/4} + Zn_{1/5}O6_{1/3} + P1_{1/4}O1_{1/3} + P1_{1/4}O2_{1/4} + P1_{1/4}O4_{1/2} + P1_{1/4}O5_{1/4} + P2_{1/4}O3_{1/4} + P2_{1/4}O4_{1/2} + P2_{1/4}O6_{1/3} + P2_{1/4}O7_{1/2}$.

Lattice energy stands for the combination ability of cations and anions of complex crystals, in which larger lattice energy corresponds to the stronger binding ability.[26] Further research on lattice energy is not only helpful to explore the crystal structure, but also meaningful to investigate the intrinsic dielectric loss. The total lattice energy (U_{total}) consists of the lattice energy of each chemical bond μ, divided into

the covalent part (U^{μ}_{bc}) and ionic part (U^{μ}_{bi}), which can be estimated as follows [27]:

$$U_{total} = \sum_{\mu} (U^{\mu}_{bc} + U^{\mu}_{bi}) \tag{6}$$

$$U^{\mu}_{bc} = 2100m \frac{\left(Z^{\mu}_{+}\right)^{1.64}}{(d^{\mu})^{0.75}} f^{\mu}_{c} \tag{7}$$

$$U^{\mu}_{bi} = 1270 \frac{(m+n) Z^{\mu}_{+} Z^{\mu}_{-}}{d^{\mu}} \left(1 - \frac{0.4}{d^{\mu}}\right) f^{\mu}_{i} \tag{8}$$

where Z^{μ}_{+} and Z^{μ}_{-} are the valence states of cations and anions in each bond μ, respectively. m and n are obtained by the bond formula. f^{μ}_{i}, f^{μ}_{c} and d^{μ} are ionicity, covalency, and bond length. As shown in Figure 9A, measured *Qf* values went through an increment from 56170 GHz to 84760 GHz and then followed a decline, similar to the changing trend of the total lattice energy. According to XRD and SEM analyses, all the ceramics were densified and remained pure phase. Thus, the *Qf* value was mainly affected by the intrinsic loss that was related to anharmonic vibration. Larger lattice energy led to the weaker lattice vibration, corresponding to a low intrinsic loss.

To evaluate the temperature coefficient τ_f, the structure stability of ceramics was considered. Bond energy *E* is a dominant index that reflects the stability of structure.[28]

$$E = \sum_{\mu} (t_c E^{\mu}_{c} + t_i E^{\mu}_{i}) \tag{9}$$

$$E^{\mu}_{c} = \frac{(r_{cA} + r_{cB})}{d^{\mu}} (E_{A-A} E_{B-B})^{0.5} \tag{10}$$

$$E^{\mu}_{i} = \frac{33200}{d^{\mu}} \tag{11}$$

where t_c and t_i are the covalent and ionic coefficient, related to electronegativity. r_{cA} and r_{cB} are the covalent radii. Here, $E_{Ba\text{-}Ba}$ = 44 kJ/mol, $E_{Zn\text{-}Zn}$ = 22 kJ/mol, $E_{Mg\text{-}Mg}$ = 11.3 kJ/mol, $E_{P\text{-}P}$ = 220 kJ/mol, and $E_{O\text{-}O}$ = 497.38 kJ/mol.[29,30] The variations in the τ_f value and total bond energy are exhibited in Figure 9B. A similar change in the two parameters suggested that a crystal with a higher *E* value was more stable, corresponding to a lower $|\tau_f|$ value.

Table 3 lists the performance of reported low-permittivity ceramics.[8,13,31-38] In comparison with the literature,[13] we obtained $BaZnP_2O_7$ and $BaZn_{0.98}Mg_{0.02}P_2O_7$ ceramics with competitive *Qf* values. However, the negative τ_f value limited the commercial application of the $BaZn_{0.98}Mg_{0.02}P_2O_7$ ceramic. TiO_2 and $CaTiO_3$ are often used as a τ_f compensator because their τ_f values are +450 ppm/°C [39] and +859 ppm/°C,[40] respectively. We propose to add TiO_2/$CaTiO_3$ in the $BaZn_{0.98}Mg_{0.02}P_2O_7$ ceramic to achieve a near zero τ_f value in future work.

Since the $BaZn_{0.98}Mg_{0.02}P_2O_7$ ceramic possessed a low sintering temperature (900°C) which made it possible for LTCC applications,[41,42] it was necessary to study whether the $BaZn_{0.98}Mg_{0.02}P_2O_7$ ceramic was chemically compatible with Ag electrode. XRD analysis confirmed that no new crystalline phases were formed for the $BaZn_{0.98}$ $Mg_{0.02}P_2O_7$ ceramic co-fired with Ag slurry, as shown in Figure 10A. The cross-sectional backscattered electron image and EDS linear scanning results are displayed in Figure 10B. Obviously, the boundary between Ag and ceramic was clearly visible and Ag presented almost no diffusion across the interface. The superior dielectric properties, a low sintering temperature, and good compatibility with Ag enabled

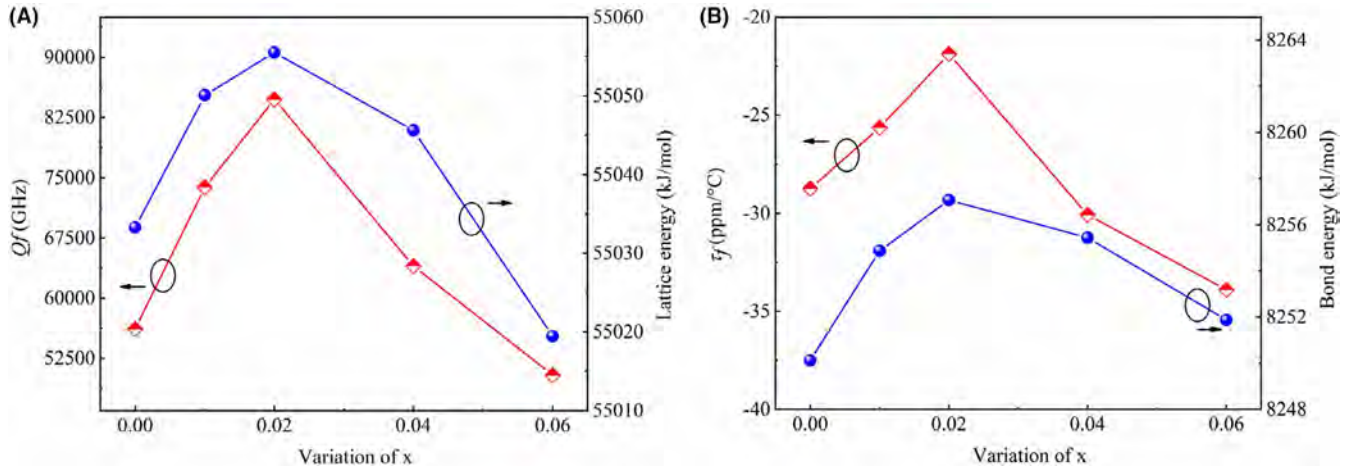

FIGURE 9 (A) The variation of *Qf* and total lattice energy with x from 0 to 0.06; (B) The variation of τ_f and total bond energy with x from 0 to 0.06

TABLE 3 Microwave dielectric properties of some low-permittivity ceramics

Composition	ST (°C)	ε_r	Qf (GHz)	τ_f (ppm/°C)	Reference
$Mn_2P_2O_7$	1100	7.34	23 850	−95.8	[8]
$CaMgSi_2O_6$	1290	7.46	59 640	−46	[31]
Nd_2SiO_5	1500	7.94	38 800	−53	[32]
YPO_4	1600	8.0	67 930	−35.3	[33]
$SrWO_4$	1150	8.1	56 000	−55	[34]
$BaZnP_2O_7$	870	8.23	56 170	−28.7	This work
$BaMg_{0.98}Zn_{0.02}P_2O_7$	900	8.21	84 760	−21.9	This work
$BaZnP_2O_7$	875	8.4	27 925	−56.7	[13]
$BaCu_{1.85}Co_{0.15}Si_2O_7$	1000	8.45	58 960	−34.4	[35]
$Ca_5Mg_4(VO_4)_6$	800	9.2	53 300	−50	[36]
$Li_3AlMo_3O_{12}$	570	9.5	50 000	−73	[37]
$Mg_{0.94}Na_{0.12}WO_4$	875	10.47	45 870	−69	[38]
$Li_2Zn_2Mo_3O_{12}$	630	11.1	70 000	−90	[37]

Abbreviation: ST: sintering temperature

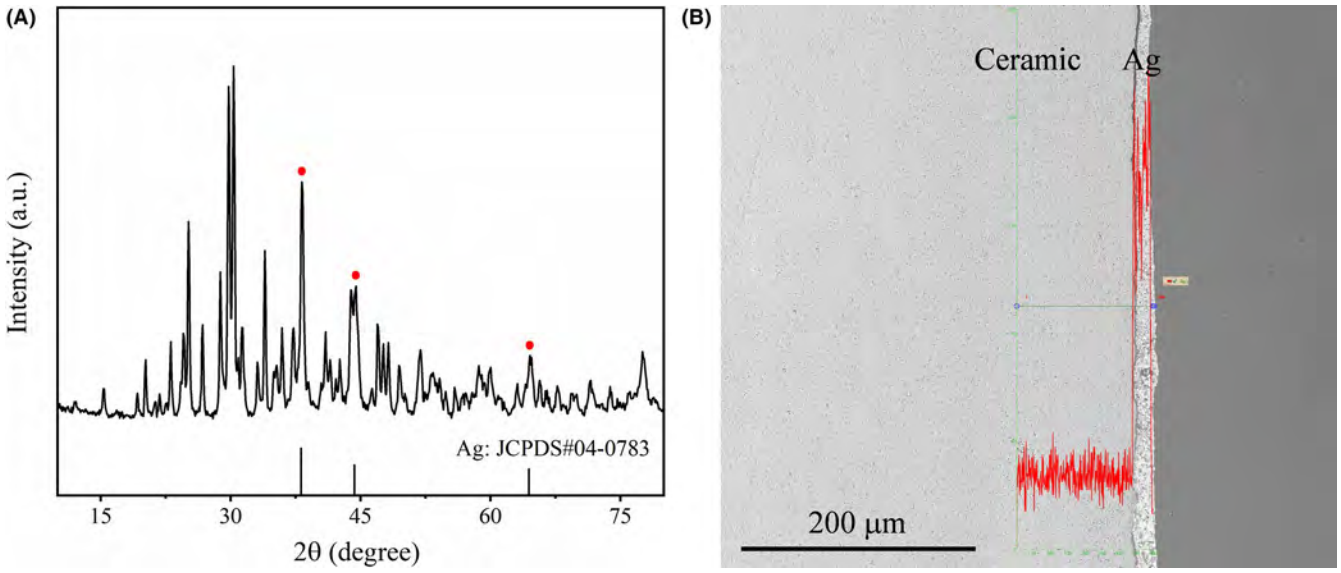

FIGURE 10 (A) The XRD pattern of the $BaZn_{0\cdot98}Mg_{0.02}P_2O_7$ ceramic brushed with Ag slurry on the surface; (B) The cross-sectional backscattered electron image and EDS linear scanning results of the $BaZn_{0\cdot98}Mg_{0.02}P_2O_7$ ceramic brushed with Ag slurry on the surface. The sample was co-fired at 900°C

the $BaZn_{0\cdot98}Mg_{0.02}P_2O_7$ ceramic to be a promising candidate for LTCC applications.

4 | CONCLUSIONS

$BaZnP_2O_7$ ceramics were prepared via solid-state synthesis. XRD and TEM results suggested that $BaZnP_2O_7$ belonged to the triclinic P−1 space group. The $BaZnP_2O_7$ ceramic sintered at 870°C for 4 h possessed a low ε_r of 8.23, a high Qf of 56170 GHz (~12 GHz), and a τ_f of −28.7 ppm/°C. It was found that dielectric constant and loss of $BaZnP_2O_7$ ceramics sintered at different sintering temperatures were highly dependent on relative density. Besides, we studied the substitution effect of Mg^{2+} at Zn site, and found that grain morphology and dielectric properties were greatly optimized. The optimum performance of ε_r = 8.21, Qf =84760 GHz and τ_f = −21.9 ppm/°C was obtained for the $BaZn_{0\cdot98}Mg_{0.02}P_2O_7$ ceramic sintered at 900°C. Clausius–Mossotti equation and complex chemical bond theory provided a deep insight into the structure–property relationship in $BaZn_{1-x}Mg_xP_2O_7$ ceramics.

ORCID

Hao Li https://orcid.org/0000-0002-9298-7898

REFERENCES

1. Dai QL, Zuo RZ. A novel ultralow-loss Sr_2CeO_4 microwave dielectric ceramic and its property modification. J Eur Ceram Soc. 2019;39:1132–6.
2. Zhou D, Li J, Pang LX, Wang DW, Reaney IM. Novel water insoluble $(Na_xAg_{2-x})MoO_4$ (0<x<2) microwave dielectric ceramics with spinel structure sintered at 410 degrees. J Mater Chem C. 2017;5:6086–91.
3. Wang D, Li L, Jiang J, Lu Z, Wang GE, Song K, et al. Cold sintering of microwave dielectric ceramics and devices. J Mater Res. 2021;36:333–49.
4. Zhou D, Li J, Pang LX, Chen GH, Qi ZM, Wang DW, et al. Crystal structure, infrared spectra, and microwave dielectric properties of temperature-stable zircon-type (Y, Bi)V_O4 solid solution ceramics. ACS Omega. 2016;1:963–70.
5. Song XQ, Lu WZ, Wang XC, Wang XH, Fan GF, Muhammad R, et al. Sintering behaviour and microwave dielectric properties of $BaAl_{2-2x}(ZnSi)_xSi_2O_8$ ceramics. J Eur Ceram Soc. 2018;38:1529–34.
6. Yin CZ, Li CC, Yang GJ, Fang L, Yuan YH, Shu LL, et al. $NaCa_4V_5O_{17}$: a low-firing microwave dielectric ceramic with low permittivity and chemical compatibility with silver for LTCC applications. J Eur Ceram Soc. 2020;40:386–90.
7. Brown ID, Calvo C. The crystal chemistry of large cation dichromates, pyrophosphates, and related compounds with stoichiometry $X_2Y_2O_7$. J Solid State Chem. 1970;1:173–9.
8. Bian JJ, Kim DW, Hong KS. Microwave dielectric properties of $A_2P_2O_7$ (A = Ca, Sr, Ba; Mg, Zn, Mn). Jpn J Appl Phys. 2004;43:3521–5.
9. Sutapun M, Muanghlua R, Niemcharoen S, Vittayakorn WC, Seeharaj P, Vittayakorn N. Synthesis, characterization and dielectric properties of $Mn_{(2-x)}Zn_xP_2O_7$ ceramics. Adv Mater Res. 2013;802:12–6.
10. Bian JJ, Kim DW, Hong KS. Glass-free LTCC microwave dielectric ceramics. Mater Res Bull. 2005;40:2120–9.
11. Yang ZP, Yang GW, Wang SL, Tian J, Li PL, Li X. Luminescence and energy transfer of Eu^{2+}, Mn^{2+} in $BaZnP_2O_7$. Acta Phys Sin. 2008;57:581–5.
12. Yang ZP, Yang GW, Wang SL, Tian J, Li PL, Li X. Preparation and luminescent properties of $BaZnP_2O_7$: Eu^{3+} salmon pink-emitting phosphor. Chem J Chin Univ. 2007;28:1631–3.
13. Xie HD, Chen C, Su BB, Xi HH. Microwave dielectric properties of low ε_r $BaZnP_2O_7$ ceramic. Mater Lett. 2016;166:167–70.
14. Verhoeven JAT, Doveren HV. XPS studies on Ba, BaO and the oxidation of Ba. Appl Surf Sci. 1980;5:361–73.
15. Wöll C. The chemistry and physics of zinc oxide surfaces. Prog Surf Sci. 2007;82:55–120.
16. Biesinger MC, Lau LWM, Gerson AR, Smart RSC. Resolving surface chemical states in XPS analysis of first row transition metals, oxides and hydroxides: Sc, Ti, V, Cu and Zn. Appl Surf Sci. 2010;257:887–98.
17. Baggetto L, Dudney NJ, Veith GM. Surface chemistry of metal oxide coated lithium manganese nickel oxide thin film cathodes studied by XPS. Electrochim Acta. 2013;90:135–47.
18. Penn SJ, Alford NM, Templeton A, Wang X, Xu M, Reece M, et al. Effect of porosity and grain size on the microwave dielectric properties of sintered alumina. J Am Ceram Soc. 1997;80:1885–8.
19. Kucheiko S, Choi JW, Kim HJ, Jung HJ. Microwave dielectric properties of $CaTiO_3$-$Ca(Al_{1/2}Ta_{1/2})O_3$. J Am Ceram Soc. 1996;79:2739–43.
20. Chen XQ, Li H, Zhang PC, Hu HL, Tao Y, Li GS. $SrZnV_2O_7$: a low-firing microwave dielectric ceramic with high quality factor. J Am Ceram Soc. 2021;00:1–10.
21. Li CC, Xiang HC, Xu MY, Tang Y, Fang L. Li_2AGeO_4 (A = Zn, Mg): two novel low-permittivity microwave dielectric ceramics with olivine structure. J Eur Ceram Soc. 2018;38:1524–8.
22. Chen JQ, Tang Y, Xiang HC, Fang L, Porwal H, Li CC. Microwave dielectric properties and infrared reflectivity spectra analysis of two novel low-firing $AgCa_2B_2V_3O_{12}$ (B = Mg, Zn) ceramics with garnet structure. J Eur Ceram Soc. 2018;38:4670–6.
23. Shannon RD. Dielectric polarizabilities of ions in oxides and fluorides. J Appl Phys. 1993;73:348–66.
24. Shannon RD, Rossman GR. Dielectric constants of silicate garnets and the oxide additivity rule. Am Mineral. 1992;77:94–100.
25. Wu ZJ, Meng QB, Zhang SY. Semiempirical study on the valences of Cu and bond covalency in $Y_{1-x}Ca_xBa_2Cu_3O_{6+y}$. Phys Rev B. 1998;58:958–62.
26. Zhang P, Zhao YG, Wu HT. Bond ionicity, lattice energy, bond energy and microwave dielectric properties of $ZnZr(Nb_{1-x}A_x)_2O_8$ (A = Ta, Sb) ceramics. Dalton Trans. 2015;44:16684–93.
27. Yang HC, Zhang SR, Yang HY, Yuan Y, Li EZ. Vibrational spectroscopic and crystal chemical analyses of double perovskite Y_2MgTiO_6 microwave dielectric ceramics. J Am Ceram Soc. 2020;103:1121–30.
28. Zhao YG, Zhang P. Influence of Ta substitution for Nb in $Zn_3Nb_2O_8$ and the impact on the crystal structure and microwave dielectric properties. Dalton Trans. 2016;45:11807–16.
29. Kildahl NK. Bond energy data summarized. J Chem Educ. 1995;72:423–4.
30. Luo YR. Comprehensive handbook of chemical bond energies. Boca Raton, FL: CRC Press. 2007. p. 255–1484.
31. Sun HP, Zhang QL, Yang H, Zou JL. $(Ca_{1-x}Mg_x)SiO_3$: a low-permittivity microwave dielectric ceramic system. Mater Sci Eng B. 2007;138:46–50.
32. Jiang C, Wu SP, Ma Q, Mei YX. Synthesis and microwave dielectric properties of Nd_2SiO_5 ceramics. J Alloy Compd. 2012;544:141–4.
33. Cho IS, Choi GK, An JS, Kim JR, Hong KS. Sintering, microstructure and microwave dielectric properties of rare earth orthophosphates, $RePO_4$ (Re = La, Ce, Nd, Sm, Tb, Dy, Y, Yb). Mater Res Bull. 2009;44:173–8.
34. Yoon SH, Kim DW, Cho SY, Hong KS. Investigation of the relations between structure and microwave dielectric properties of divalent metal tungstate compounds. J Eur Ceram Soc. 2006;26:2051–4.
35. Song XQ, Lu WZ, Lou YH, Chen T, Ta SW, Fu ZX, et al. Synthesis, lattice energy and microwave dielectric properties of $BaCu_{2-x}Co_xSi_2O_7$ ceramics. J Eur Ceram Soc. 2020;40:3035–41.
36. Yao GG, Liu P, Zhang HW. Novel Series of Low-Firing Microwave Dielectric Ceramics: $Ca_5A_4(VO_4)_6$ (A^{2+} = Mg, Zn). J Am Ceram Soc. 2013;96:1691–3.
37. Zhou DI, Randall CA, Pang L-X, Wang H, Wu X-G, Guo J, et al. Microwave dielectric properties of $Li_2(M^{2+})_2Mo_3O_{12}$ and $Li_3(M^{3+})Mo_3O_{12}$ (M = Zn, Ca, Al, and In) lyonsite-related-type ceramics with ultra-low sintering temperatures. J Am Ceram Soc. 2011;94:802–5.
38. Zhang Q, Tang XL, Li YX, Jing YL, Su H. Influence of substituting Na^+ for Mg^{2+} on the crystal structure and microwave

dielectric properties of $Mg_{1-x}Na_{2x}WO_4$ ceramics. J Eur Ceram Soc. 2020;40:4503–8.

39. Guo YP, Ohsato H, Kakimoto KI. Characterization and dielectric behavior of willemite and TiO_2-doped willemite ceramics at millimeter-wave frequency. J Eur Ceram Soc. 2006;26:1827–30.
40. Subramanian V, Murthy VRK, Viswanathnan B. Microwave dielectric properties of certain simple alkaline earth perovskite compounds as a function of tolerance factor. Jpn J Appl.Phys. 1997;36:194–7.
41. Guo HH, Fu MS, Zhou D, Du C, Wang PJ, Pang LX, et al. Design of a high-efficiency and -gain antenna using novel low-loss, temperature-stable $Li_2Ti_{1-x}(Cu_{1/3}Nb_{2/3})_xO_3$ microwave dielectric ceramics. ACS Appl. Mater Interfaces. 2021;13:912–23.
42. Guo HH, Zhou D, Du C, Wang PJ, Liu WF, Pang LX, et al. Temperature stable $Li_2Ti_{0.75}(Mg_{1/3}Nb_{2/3})_{0.25}O_3$-based microwave dielectric ceramics with low sintering temperature and ultra-low dielectric loss for dielectric resonator antenna applications. J Mater Chem C. 2020;8:4690–700.

How to cite this article: Chen X, Li H, Zhang P, Hu H, Chen G, Li G. A low-permittivity microwave dielectric ceramic $BaZnP_2O_7$ and its performance modification. *J Am Ceram Soc*. 2021;00:1–10. https://doi.org/10.1111/jace.17839